Combining in-line chromatography coupled SAXS and AI-predicted structures to dissect the mechanism of ParB1-*parS1* partition assembly formation

Anu[1, 2], Sneh Lata[1, 2], Barnali N. Chaudhuri[1, 2, *]

[1]GN Ramachandran Protein Center, CSIR Institute of Microbial Technology, Chandigarh 160036, India

[2]Academy of Scientific and Innovative Research (AcSIR), Ghaziabad, Uttar Pradesh 201002, India

* correspondence email: barnalichaudhuri1@gmail.com

Abstract

ParB, which is a CTP-dependent DNA clamp, is an essential component of bacterial ParABS chromosomal origin segregation apparatus. A CTP-induced conformational switching leads to a closed conformation of dimeric ParB that displaces *parS* DNA from its binding site to enable sliding. We combined in-line chromatography-coupled SAXS and AI-predicted structure of full-length ParB1 from *Vibrio cholerae* to elucidate critical conformational changes associated with ParB1-*parS1* assembly formation. Like other ParBs, ParB1 can hydrolyse CTP. In-line SAXS provided size distribution of ParB1, and showed population shift to a more compact state upon ParB1-*parS1* assembling. A truncated N-terminal segment of ParB1 devoid of the putative intrinsically unstructured regions appears to self-associate in multiple oligomeric states in solution. Imparting flexibility in a linker region joining this N-terminal segment and the C-terminal dimerization domain makes full-length ParB1 highly association-prone, implying that this linker may modulate self-interaction of vcParB1 for partition assembly condensate formation. To visualize the clamping-related conformational states, integrative models of full-length ParB1 and *parS1*-bound ParB1 were built by combining SAXS profiles with Alphafold2 models. Resultant integrative structural models revealed *parS1*-induced conformational changes in ParB1 at the onset of clamp formation.

Introduction

Segregation of bacterial chromosomal origin region is driven by ParABS partition cassette, or segrosome, in many bacteria (Funnell, 2016; Jalal and Le, 2020; Tisma et al, 2024). ParABS cassette is a three-component system consisting of ParA, ParB and one or more short, ParB-binding palindromic *parS* site(s) near the chromosomal origin (Funnell, 2016; Jalal and Le, 2020; Tisma et al, 2024; Livny et al., 2007). ParA is an ATPase that non-specifically binds DNA and reportedly forms a gradient on the nucleoid across the cell (Vecchiarelli et al., 2014). ParB is a CTPase that acts as a DNA clamp (Osorio-Valeriano et al., 2019; Soh et al., 2019; Osorio-Valeriano et al., 2021). Multiple ParBs can spread around the *parS* site(s) to form a large partition assembly probably by both sliding on the DNA and DNA bridging (Sanchez et al., 2015; Funnell, 2016; Jalal and Le, 2020; Walter et al., 2020; Balaguer et al., 2021; Antar et al., 2021; Guo et al., 2022; Tisma et al., 2022; Tisma et al, 2023; Tisma et al, 2024). Partition assembly follows intracellular ParA gradient during chromosomal origin segregation (Vecchiarelli et al., 2014), and also participate in loading of 'Structural Maintenance of Chromosome' (SMC) proteins on DNA (Sullivan et al., 2009; Bock et al., 2022). Earlier, a number of mechanisms of origin segregation have been proposed (Ptacin et al., 2010; Lim et al., 2014; Vecchiarelli et al., 2014). Recently it was reported that ParB can from liquid-liquid phase separated condensates (LLPS) both *in vivo* and *in vitro*, which are regulated by CTP (Guilhas et al., 2020; Babl et al., 2022). The biological roles of these condensates in ParB-mediated DNA segregation are just beginning to emerge (Guilhas et al., 2020; Babl et al., 2022; Azaldegui et al., 2021).

A canonical ParB is dimer containing three domains (Funnell, 2016; Jalal and Le, 2020). The N-terminal domain of ParB binds and hydrolyses CTP (CTP-binding domain or CTPBD, Osorio-Valeriano et al., 2019; Soh et al., 2019). A central helix-turn-helix motif-containing domain (HTHD) specifically binds palindromic *parS* DNA (Jalal et al., 2020). The C-terminal dimerization domain (CTDD) of ParB harbours a weak DNA-binding site (Fisher et al., 2017). Recent crystal structures of the nucleotide-bound and *parS*-bound truncated versions of ParB from a number of bacteria aided in understanding the CTP-dependent DNA clamping mechanism (Osorio-Valeriano et al., 2019; Soh et al., 2019; Jalal et al., 2020; Jalal et al., 2021; Osorio-Valeriano et al., 2021). It has been proposed that binding of two nucleotides at the dimer interface of CTPBD forms a locked "N-gate", thus forming a closed vcParB1 clamp (Osorio-Valeriano et al., 2019; Soh et al., 2019; Jalal et al., 2020). This CTP-induced "N-gate" closure displaces *parS* DNA from the central HTHD, which is critical for sliding of the ParB clamp on DNA. At the same time, CTP hydrolysis is catalysed by *parS*, suggesting a coupled conformational change in ParB (Jalal and Le, 2020). Structures of the full-length ParB in various conformational states, that are critical for understanding the domain rearrangements required for clamping-sliding process, has not been determined.

Artificial intelligence (AI) based structure prediction programs, such as Alphafold2, are now widely used, convenient tools for predicting 3-dimensional structures of folded proteins, including multi-domain and multimeric proteins, from primary sequences (Jumper et al., 2021; Mirdita et al., 2022). However, these predicted structures provide only one conformation. Interconversions between conformational states associated with different stimuli are critical for functioning of

protein switches, such as ParB CTP switch (Alberstein et al., 2022, McLean. and Le, 2023). These conformational states cannot be immediately deduced from one AI-predicted static structure. Experimental small angle solution X-ray scattering (SAXS) data can be suitably combined with these AI-predicted structures for modelling conformational states associated with protein function (Brookes et al., 2023). Advanced methodologies, such as size exclusion column chromatography coupled SAXS (SEC-SAXS, Mathew et al., 2004), and evolving factor analysis (EFA, Meisburger et al., 2016), can be particularly useful for separating scattering profile of the assembly component from SAXS data obtained from a mixture of components. These methods can aid in better structural modelling of conformational states of multimeric assemblies, including nucleoprotein assemblies. In addition, SAXS is a fitting tool for probing molecular features of proteins that potentially contribute to LLPS formation (Martin et al., 2021).

Here, we combined SEC-SAXS and AI-predicted structures to build integrative or hybrid models to understand the mechanism of interaction between ParB1 from *Vibrio cholerae* (vcParB1) and cognate *parS1* (Fogel and Waldor, 2005; Yamaichi et al., 2007; Ramachandran et al., 2014). We show that vcParB1 is a CTP-hydrolysing, *parS1*-binding enzyme. Comparison of the integrative models of dimeric free vcParB1 and vcParb1-*parS1* complex show large scale conformational changes upon DNA binding, leading to repositioning of the CTPBD and formation of a lumen region below *parS1*-binding site. Both vcParB1 and CTP-treated vcParB1 adopts open conformations in solution. In addition, our data reveals that a truncated vcParB1 construct containing the CTPBD and HTHD, and none of the putative intrinsically unstructured regions, can form a heterogeneous mixture of oligomeric states. A flexible linker region joining the CTDD and HTHD appears to restrain the overall self-associating tendency of full-length vcParB1. DNA-induced conformational changes and self-interacting properties of vcParB1 are discussed in the context of clamping-sliding and large partition-assembly condensate forming functions of vcParB1.

Materials and Methods

Protein expression and purification

Sources of constructs used in this study are listed in supplementary material **S1**. Either pET15b or pET28a vectors containing genes of target proteins were transformed into BL21(DE3) competent cells. Cells were grown at 37° C in Luria-Bertani broth (Difco, Fisher scientific, cat 244620) with added antibiotics (100 µg/ml of ampicillin, Sisco Research Laboratory, cat 61314 or 50 µg/ml kanamycin monosulfate, Gold Biotechnology, cat K-120-5) till OD_{600} reached 0.6. Next, Isopropyl-β-D-thiogalactoside (IPTG, 1 mM; Gold Biotechnology, cat I2481C50) was used for induction and cells were grown for another 15 hours at 25° C. Cells were harvested and stored at - 80° C.

For protein purification, cells were lysed by sonication (Sonics Vibra-Cell, VCX750, Sonics & Material) in the lysis buffer containing 100 mM Tris.HCl (Sigma-Aldrich cat T6066) pH 7.5, 1 M NaCl (Sigma-Aldrich cat S3014), 5 % glycerol (Sigma-Aldrich cat G7757), 5 mM β-mercaptoethanol (BME, Sigma-Aldrich cat M6250), 0.2 mM ethylenediaminetetraacetic acid (EDTA, Sigma-Aldrich cat EDS)

and protease inhibitor cocktail (Sigma-Aldrich, cat P8849). Proteins were purified using immobilized metal affinity column chromatography (IMAC sepharose 6 fast flow, Cytiva, cat 17092107), followed by ion exchange column chromatography (Q sepharose Fast Flow, Cytiva, cat 17051010) and size-exclusion column chromatography (SEC; HiLoad 16/600 Superdex 200 pg, Cytiva, cat 28989335). Proteins were loaded to Ni^{+2}-charged IMAC sepharose fast flow column in lysis buffer. Unbound and weakly bound proteins were eluted by wash buffer (20 mM Tris.HCl pH 7.5, 1 M NaCl, 5 % glycerol), followed by a binding buffer containing 20 mM Tris.HCl pH 7.5, 300 mM NaCl, 5 % glycerol and 20 mM imidazole (Sigma-Aldrich cat I2399). Bound proteins were eluted in the binding buffer with increased concentration of imidazole in steps up to a maximum concentration of 500 mM. Next, the collected protein fractions were pulled and dialysed in the ion exchange buffer (20 mM Tris.HCl pH 7.5, 20 mM NaCl, 5 mM BME, 5 % glycerol, 1 mM EDTA). A gradient of 20 mM to 500 mM NaCl was used for eluting the protein. Buffer for the size-exclusion column chromatography run contained 20 mM Tris.HCl pH 7.5, 100 mM NaCl, 5% glycerol, 5 mM BME and 1 mM EDTA (**Figure S1**). Purity levels of the proteins were evaluated by sodium dodecyl sulfate-polyacrylamide gel electrophoresis (SDS-PAGE). Fractions from the peak region were collected and further concentrated. Trypsin digested (in-gel digestion, Trypsin singles, proteomics grade, cat T7575) proteins were further confirmed by MS/MS ion search from one or more peptides in MASCOT database server (Perkins *et al*, 1999). Protein concentrations were determined using BCA assay (Pierce BCA protein assay kit, cat 23225).

Oligonucleotide preparation

Commercially synthesized oligonucleotides were obtained in PAGE-purified form from Sigma-Aldrich oligonucleotide synthesis facility (supplementary material **S1**). Equimolar concentrations of oligonucleotides were mixed and annealed by heating at 95°C (10 minutes), followed by cooling at room temperature (45 minutes) and at 4°C (overnight).

Plasmids with and without *parS1* site (pUC57, supplementary material **S1**) were transformed into TOP10 cells (Invitrogen, cat C404003), grown in LB media with appropriate antibiotics, and extracted by GeneJET plasmid miniprep kit (Thermo Scientific).

CTPase activity assay

To detect CTPase activity of vcParB1, malachite green assay (Malachite green oxalate salt, Sigma-Aldrich, cat M6880, Ammonium molybdate tetrahydrate, Sigma, cat 09878) was performed. Standard curves were prepared using potassium phosphate monobasic (Sigma Aldrich, cat P5379). Protein (8 μM) and cytidine triphosphate (CTP; Thermo scientific, cat R0451, 1 mM) were incubated in the reaction buffer (20 mM Tris.HCl pH 7.5, 150 mM NaCl, 5 mM $MgCl_2$) for 60 minutes at room temperature. OD_{650} was measured in a plate reader (Thermo Fisher scientific, Multiskan Go) after adding the malachite green working reagent and sodium citrate. Reaction buffer with CTP was used as blank for subtraction. Next, these experiments were repeated in the presence of oligonucleotides (1 μM *parS1* or 1 μM *nsDNA16*) and 1 μg pUC57 plasmid (with or without a *parS1* sequence)

(supplementary material **S1**). All experiments were performed four times and plotted in Excel (Microsoft).

Biolayer interferometry

ParB1-DNA interactions were detected by biolayer interferometry in our in-house Octet K2 (ForteBio, USA). Biotinylated duplex DNA (bt-*parS1*, Supplementary material **S1**) containing a single *parS1* sequence, and non-specific DNA (bt-*nsDNA*), were used for coating streptavidin biosensor (SA biosensor, Sartorius). Protein concentrations were optimized before the final runs in the reaction buffer containing 50 mM Tris.HCl pH 8.0, 150 mM NaCl, 5 mM $MgCl_2$, 1 mM BME, 0.05 % Tween20 (Sigma-Aldrich, cat P9416), 0.5 % Bovine Serum Albumin (Sigma-Aldrich, cat A2153). All experiments were done in triplicate. Data analysis was performed using the software Data Analysis HT 11.1 (Sartorius). A heterogeneous binding model was used for data analysis that provided two on-rates and two off-rates. It was not possible to obtain reliable dissociation constant due to much variability in the data, which is probably due to the self-associating nature of vcParB1.

SAXS and SEC-SAXS experiments

Purified proteins and protein-DNA complexes were snap-frozen under liquid nitrogen and shipped to the synchrotron beamline in a dry shipper. All data were collected at the beamline BM29, European Synchrotron radiation facility (ESRF), Grenoble, France (Tully et al., 2023). Experimental parameters are presented in **Table 1**.

SAXS and SEC-SAXS data analysis

Resultant SAXS and SEC-SAXS data were analysed using BioXTAS RAW 2.2.1 (Hopkins, 2024) and ATSAS suite of software (Manalastas-Cantos et al., 2021). Following buffer subtraction, peak regions of protein and protein-DNA complexes from the SEC-SAXS elution profiles were selected based on singular value decomposition (SVD) analysis using BIOXTAS RAW (**Figure S2**; Hopkins, 2024). Averaged scattering profiles were used for subsequent analysis (**Figure S3**). Regularized alternating least squares (REGALS; Meisburger et al., 2021) analysis was performed for the SEC-SAXS dataset of the vcParB1-*parS1* complex. Pair distribution functions were calculated using GNOM (Manalastas-Cantos et al., 2021). Second virial coefficients (B22) were estimated from concentration series of batch mode SAXS data (Pabit et al., 2009), using the following equation –

$$\frac{1}{I(c,0)} = \frac{1}{F(0)} + \frac{2.M.B22.c}{F(0)} \qquad (1)$$

I(c,0) is the forward scattering intensity at concentration c, M is mass and F(0) is form factor at 0 scattering angle. CRYSOL was used for calculating theoretical scattering profiles from atomic coordinates (Manalastas-Cantos et al., 2021). Excel (Microsoft) was used for preparing the graphs and analysing data.

AI-based structure prediction

Structural models of full-length, dimeric vcParB1 were obtained from Colabfold (Jumper et al., 2021; Mirdita et al., 2022), using Alphafold Multimer v3 option with custom templates. Known crystal structures of C-terminally truncated ParB from *Caulobacter vibrioides* (cvParBtrunc, ~ 39 % sequence identity with vcParB1 for residue coverage of ~ 76 %) in nucleotide-bound form (pdb code: 7bm8, Jalal et al., 2021) and *parS*-bound form (pdb code: 6t1f, Jalal et al., 2021) were used as templates for two runs. Top ranking predicted structures from these runs were subsequently used for SAXS-based structural modelling.

Integrative structural modelling and analysis

CORAL (Petoukhov et al., 2012) from the ATSAS suite version 3.3.0-prerelease (Manalastas-Cantos et al., 2021) was used for SAXS-dependent structural modelling using averaged experimental scattering profiles. Strict two-fold symmetry was imposed for all CORAL runs. Rigid bodies of CTPBD (37-132 residues), HTHD (137-232 residues) and CTDD (239-293 residues) were used as inputs for the CORAL runs in three-domain mode. At times, combined CTPBD and HTHD (37-232 residues) and CTDD were used for CORAL runs in two-domain mode. In an attempt to improve geometry of the predicted model, positional energy minimization was performed in Phenix (Liebschner et al., 2019). Two flexible regions, that contained less than 20 % of the protein residues, were obtained from CORAL loop library (Petoukhov et al., 2012). 20 CORAL runs were performed against each dataset. Additional distance restraints between the CTDD/CTPBD dimers (based on the Alphafold2 model) and between HTHD and *parS1* DNA (based on the structure of cvParBtrunc-*parS* complex, pdb code 6t1f) were added, as required.

In addition to experimental data, theoretical scattering profiles of the dimerized domains (CTDD, HTHD and CTPBD, as required) of vcParB1 were used as supplementary synthetic data during the CORAL runs. Theoretical scattering profiles were calculated from structural models of truncated dimeric domains using CRYSOL (Manalastas-Cantos et al., 2021). Segments of the predicted Alphafold2 model of vcParB1 dimer was used for calculating theoretical profiles of the dimeric CTDD and dimeric CTPBD domains. The two HTHD domains of vcParB1 were superposed on the corresponding domains of the cvParBtrunc-*parS* complex (pdb code 6t1f) for obtaining dimeric, *parS1*-bound form of HTHD for theoretical profile calculation.

The unbound form of vcParB1 and CTP-treated vcParB1 were modelled using the experimental data, and the theoretical SAXS profile of the dimeric CTDD. Two theoretical scattering curves, one for the dimeric CTDD and one for the dimeric HTHD in *parS1*-bound form, were used along with the experimental scattering data for modelling the vcParB1-*parS1* assembly. The HTHD domain of vcParB1 was altered in *Coot* (Emsley and Cowtan, 2004) to match the HTHD of cvParBtrunc-*parS* complex (pdb code 6t1f), so that it can bind *parS1* without conflict. The *parS1* DNA model (obtained by trimming the coordinates of the *parS* duplex, pdb code 6t1f), after shifting to the origin and reorienting the two-fold axis with the Z-axis, was kept fixed during CORAL runs. For modelling CTP-treated vcParB1 in “N-gate closed” form, theoretical SAXS profiles of dimeric CTDD and dimeric CTPBD (N-gate-closed form) were used along with the experimental scattering profile.

Coot (Emsley and Cowtan, 2004) and Pymol (Schrodinger, LLC) were used for visualizing and superposing the structural models in graphics. APBS (Baker et al., 2001) was used for the calculation of electrostatic potential map. Amber charges and all default parameters were used for APBS calculations. Multiple sequence alignments were prepared in Jalview (Waterhouse *et al*, 2009). PyMol (Schrodinger, LLC) was used for preparing figures.

Data availability

SAXS and SEC-SAXS data were deposited to SASBDB databank (www.sasbdb.org), with following accession numbers:

Results

1. ParB1 is a *parS1*-binding CTPase

Recently, it has been shown that ParB is a CTPase that act as a DNA clamp (Osorio-Valeriano et al., 2019; Soh et al., 2019). The CTPase active site is located in the N-terminal domain of ParB, and contains a signatures GxxRxxA sequence motif (Soh et al., 2019; **Figure 1A**). Crystal structure of a C-terminally truncated ParB from *Bacillus subtilis* (bsParB; pdb code 6sdk, Soh et al., 2019; **Figure 1B-C**) showed two nucleotides and calcium ions bound at the dimer interface of the N-terminal CTPBD (**Figure 1B-C**). Like many other ParBs, the N-terminal region of vcParB1 contains this GxxRxxA sequence motif (**Figure 1A**). To detect CTPase activity in vcParB1, we performed malachite green assay (**Figure 1D**). Addition of *parS1*, but not non-specific DNA, appears to enhance CTPase activity of vcParB1 by a few folds (**Figure 1D**). A 16-meric DNA duplex containing the palindromic *parS1* sequence (Yamaichi et al., 2007), and a non-specific duplex DNA of equal length (*nsDNA16*) were used for our experiments (See supplementary material **S1**). A mutation in the residue N112S at the CTPase active site reportedly made bsParB hydrolysis deficient (Soh et al., 2019). A corresponding mutation (N129A) in vcParB1 reduced CTPase activity of the mutant vcParB1-N129A in comparison to the activity of wild-type vcParB1 (**Figure 1D**). A plasmid DNA (pUC57) containing a single *parS1* site appears to mildly increase the CTPase activity of vcParB1 (**Figure 1E**). Thus, the N-terminal domain of vcParB1 has CTP hydrolysing activity, which is mildly enhanced in the presence of cognate *parS1* DNA.

Figure 1.

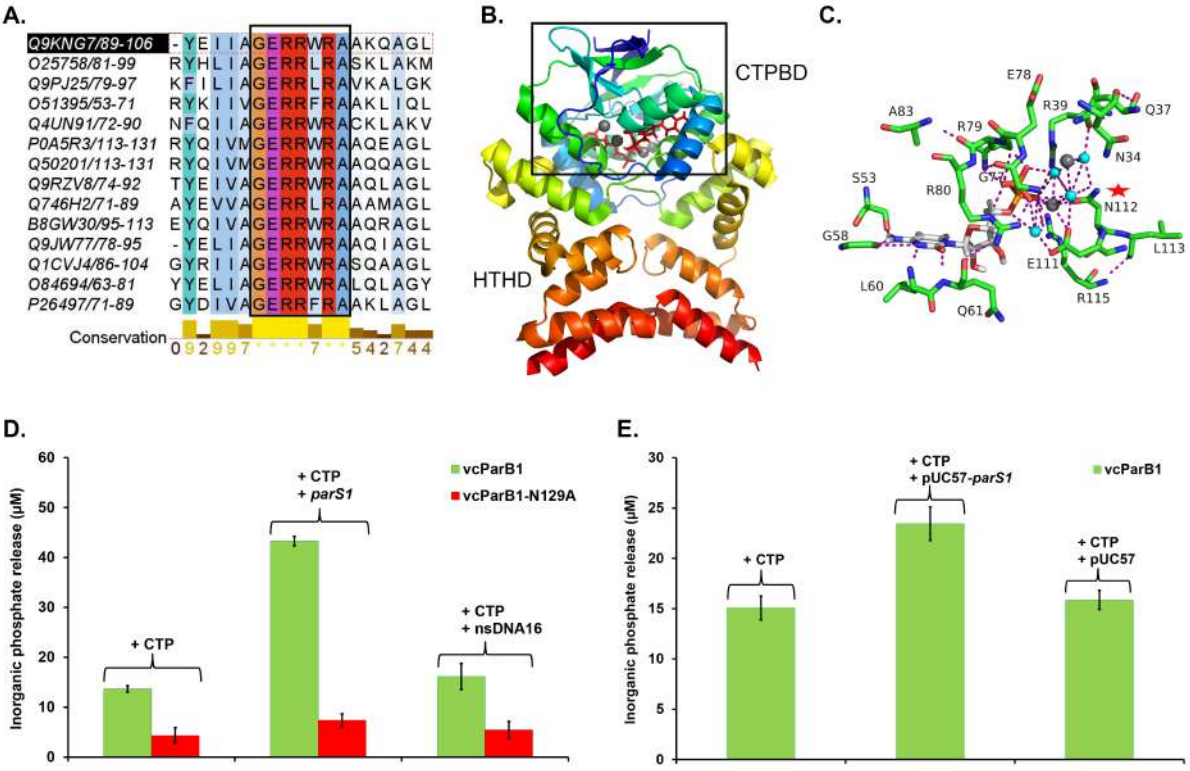

Figure 1. CTPase activity of vcParB1. (A) Multiple sequence alignment of the N-terminal region of vcParB1 (Uniprot accession number Q9KNG7, residues 89 to 106,

encompassing the conserved GxxRxxA motif) with homologous ParBs (*Helicobacter pylori*: O25758, *Campylobacter jejuni*: Q9PJ25, *Borreliella burgdorferi*: O51395, *Rickettsia felis*: Q4UN91, *Mycobacterium bovis*: P0A5R3, *Mycobacterium leprae*: Q50201, *Deinococcus radiodurans*: Q9RZV8, *Thermus thermophilius*: Q746H2, *Caulobacter vibrioides*: B8GW30, *Neisseria meningitides*: Q9JW77, *Myxococcus xanthus*: Q1CVJ4, *Chlamydia trachoatis*: O84694, *Bacillus subtilis*: P26497) is shown. (B) Truncated, dimeric bsParB CTPase is shown (Jones rainbow, pdb code: 6sdk, Soh et al., 2019), with the two bound nucleotides (red stick) and calcium ions (grey ball), as cartoon. The active site is marked with a box. (C) CTPase active site of bsParB. Active site residues are shown as sticks (with carbon in green, oxygen in red and nitrogen in blue). Bound CDP (stick, carbon in grey, oxygen in red and nitrogen in blue), calcium ion (grey ball) and water molecules (cyan ball) are shown. The N112 residue is marked with a red star. (D) Bar graph showing the result of CTPase activity assay of vcParB1 (green) and vcParB1-N129A mutant (red), with and without added specific (*parS1*) and non-specific DNA (*nsDNA16*). (E) Bar diagram showing the result of CTPase activity assay of vcParB1 in the presence and absence of pUC57 plasmid containing a single *parS1* site, and a control pUC57.

Figure 2.

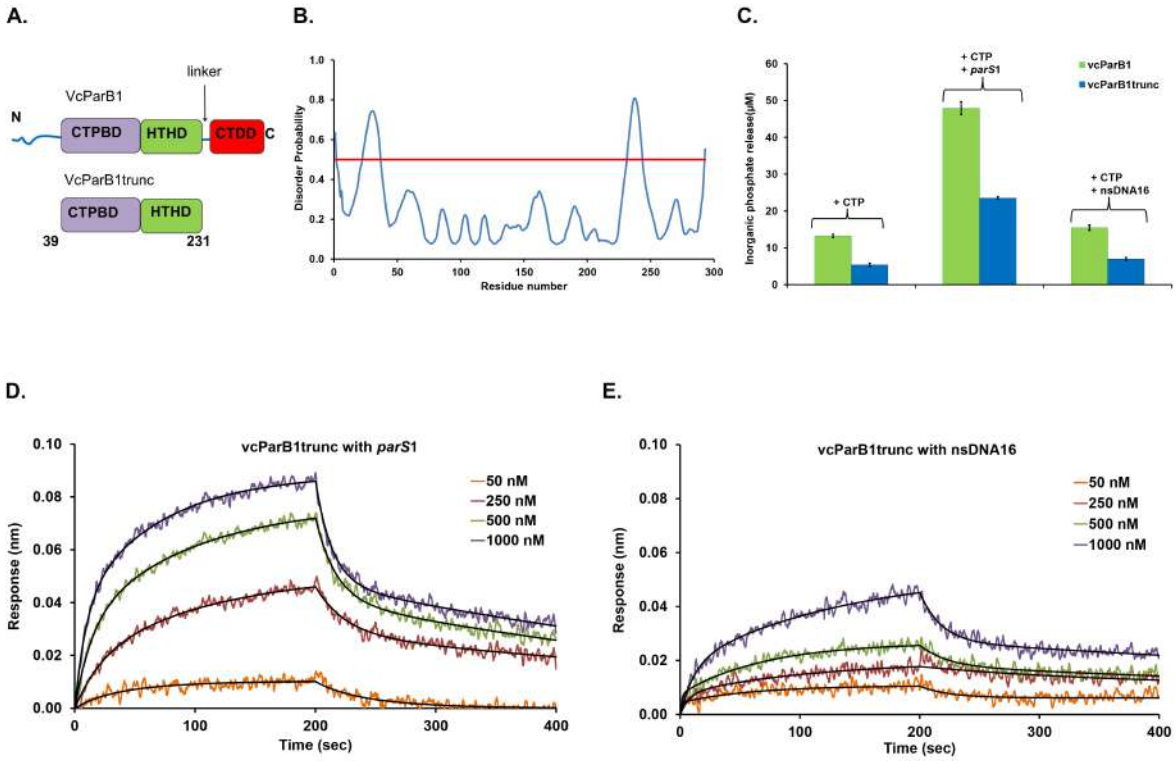

Figure 2. A truncated form of vcParB1 hydrolyses CTP and binds DNA. (A) Schematic diagram showing the domain organizations of vcParB1 and truncated vcParB1trunc. (B) Predicted intrinsic disorder (disorder probability *versus* residue number, calculated in PrDOS (prdos.hgc.jp, Takashi and Kengo, 2007) of vcParB1 plotted against residue numbers. The threshold is shown as a horizontal red line. (C) Bar graph showing the CTPase activity of vcParB1 (green), and vcParB1trunc (blue), in the presence and absence of specific and non-specific DNA. (D-E) Sensograms (response in nm *versus* time in sec) of interactions between vcParB1trunc and *parS1* (D) and nsDNA16 (E) are shown with fitted curves (black solid line).

To characterize the interaction between *parS1* and the HTHD, we prepared an N- and C-terminally truncated construct of vcParB1 (vcParB1trunc, **Figure 2A**) that contains the CTPBD and HTHD, but not the C-terminal CTDD containing the secondary DNA binding site (Fisher et al., 2017). The two predicted intrinsically unstructured regions (IDR) in vcParB1, one at the N-terminus and another short linker joining the HTHD and CTDD, were deleted in this vcParB1trunc construct (**Figure 2A-B**). Purified vcParB1trunc showed CTPase activity, which was mildly enhanced by *parS1* (**Figure 2C**). Biolayer interferometry binding assay showed that monomeric vcParB1trunc binds both specific *parS1* and non-specific *nsDNA16*, as expected (**Figure 2D-E**).

2. ParB1-*parS1* nucleoprotein assembly adopts a compact conformation

We probed vcParB1-DNA interaction using a series of SEC-SAXS runs for unbound vcParB1, unbound DNA and vcParB1-DNA assembly (**Figure 3A**). Based on the distribution of radii of gyration (R_g) values across the peak region of the vcParB1 SEC-SAXS elution profile (**Figure 3A**), as well as SVD analysis surrounding the peak region (**Figure S2A-B**), an averaged SAXS profile (vcParB1-peak) was selected. The vcParB1-peak profile was further analysed to obtain average R_g and maximum particle diameter (D_{max}) (**Table 2**).

A comparison of the SEC-SAXS elution profiles of vcParB1, vcParB1-*parS1*, vcParB1-*nsDNA16*, *parS1* and *nsDNA16*, showed that the eluted DNA peaks were well-separated from the eluted vcParB1 protein and protein-DNA complex peaks (**Figure 3A**). However, eluted peaks of vcParB1 and vcParB1-DNA complexes were overlapping (**Figure 3A**). Overall R_g distribution surrounding the peak region showed that the average size of the vcParB1-*parS1* complex, and that of the vcParB1-nsDNA16 complex to a lesser extent, is reduced when compared to the average size of vcParB1 (**Figure 3A**). This shift in R_g value is a likely indication of conformational change upon vcParB1-*parS1* assembly formation.

Next, we performed REGALS decomposition (Meisburger et al., 2021) of vcParB1-*parS1* SEC-SAXS data encompassing the peak region. REGALS analysis of vcParB1-*parS1* elution profile supported the presence of 3 components in the peak region: one major component and two other components with noisy scattering profiles (**Figure S4A-C**). The major component (vcParB1-*parS1*-deconv), which was most compact in the Kratky plot, was assigned to be the protein-DNA complex (**Figure S4A-B**). In addition, SVD analysis of the eluted vcParB1-*parS1* peak region identified presence of a segment containing one component, which was averaged (vcParB1-*parS1*-peak; **Table 2; Figure S2C-D**) and used for subsequent analysis along with the vcParB1-*parS1*-deconv profile (**Figure S3A; Table 2**). A comparison of pair distribution functions obtained from the vcParB1-*parS1*-peak/vcParB1-*parS1*-deconv and DNA-free vcParB1 profiles showed that the nucleoprotein complex is about 20 Å smaller in size than the DNA-free form of vcParB1, which is probably due to a conformational change in vcParB1 upon *parS1* binding (**Table 2; Figure 3B**).

Figure 3.

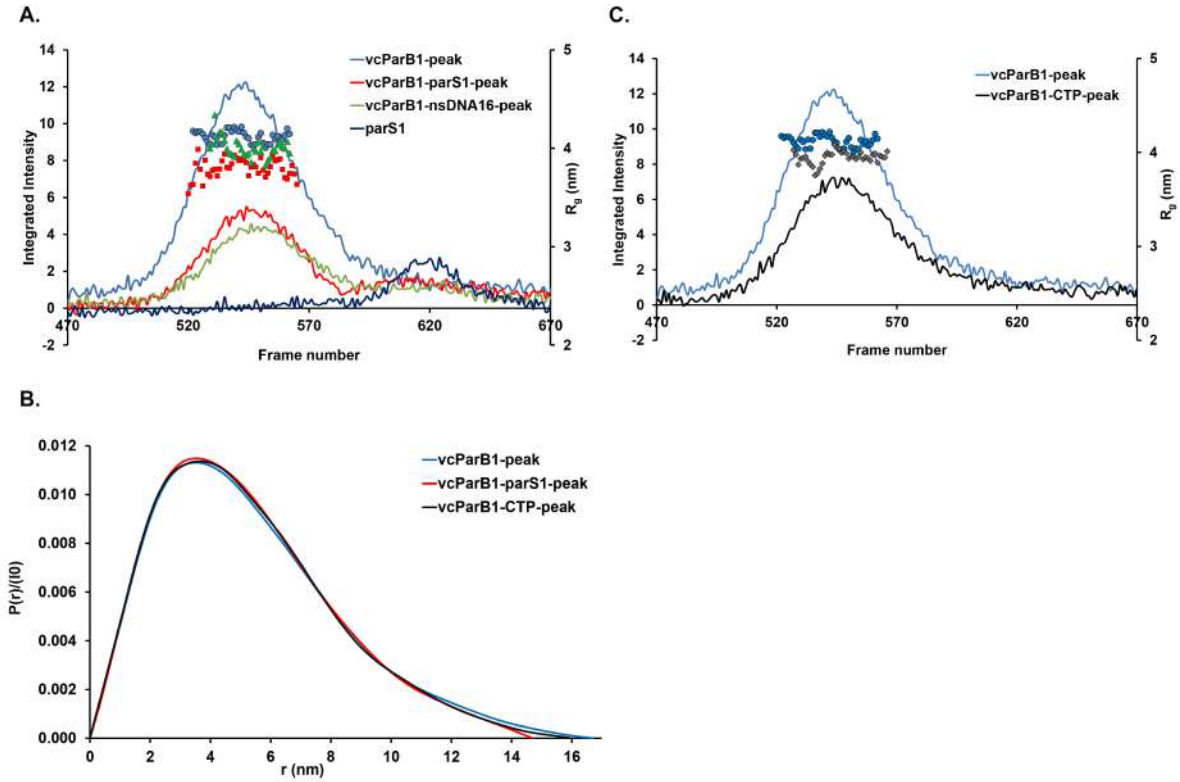

Figure 3. SEC-SAXS elution profiles of vcParB1 in free and DNA-bound states. (A) SEC-SAXS elution profiles, along with R_g distribution, for vcParB1 (solid blue line, R_g as blue circle), vcParB1-*parS1* (solid red line, R_g as red square) and vcParB1-*nsDNA16* (solid green line, R*g* as green triangle) are shown (x-axis: SEC-SAXS frame number; primary vertical axis (left): integrated intensity in arbitrary unit; secondary vertical axis (right): R_g in nm, calculated as a moving average of 5 frames in BioXTAS RAW, Hopkins, 2024). Elution profile for *parS1* DNA (dark blue solid line) is shown. Elution profile for *nsDNA16*, which elutes at the same place as *parS1*, is not shown. (B) Comparison of normalized Pair distribution functions (P(r)/I(0) *versus* r, P(r) is pair-distribution function, I(0) is forward scattering intensity and r is pairwise distance between atoms in nm; computed with boundary conditions that P(r) = 0 at r = 0 and r ≥ D_{max}) of vcParB1-peak (blue), vcParB1-*parS1*-peak (red) and vcParB1-CTP (black). (C) SEC-SAXS elution profiles of CTP-treated vcParB1 (solid black line, with R_g as grey diamond), with the vcParB1 (solid blue line, with R_g shown as blue circle) SEC-SAXS profile, plotted in the same way as in figure 3A.

To probe how the presence of nucleotide affects vcParB1 conformation, we performed SAXS experiments in batch mode with vcParB1 treated with molar excess of slowly hydrolysable CTP analog cytidine-5'-[(β,γ)-methyleno]triphosphate in the presence of divalent metal cations. The SAXS profiles obtained from these nucleotide-treated vcParB1 showed mark of aggregation. Therefore, we performed SEC-SAXS experiments with vcParB1 treated with molar excess of CTP. To keep vcParB1 saturated with nucleotide, mobile phase buffer for this SEC-SAXS run was supplemented with 1.2 mM of CTP. Distribution of R_g values of CTP-treated vcParB1, which could be a mixture of nucleotide-bound vcParB1 and unbound vcParB1, is somewhat different from that of vcParB1 (**Figure 3C**). Evolving factor analysis was not successful for these SEC-SAXS datasets. Based on the result of

SVD analyses around the peak regions (**Figure S2E-F**), averaged intensity profiles of nucleotide-treated vcParB1 (vcParB1-CTP-peak) was obtained from a set of contiguous frames for further size analysis (**Figure S3B**). Comparison of size parameters obtained from vcParB1-CTP-peak and vcParB1-peak profiles showed small reduction in overall size of the protein upon CTP binding, suggesting conformational change in vcParB1 in the presence of nucleotide (**Table 2; Figure 3B-C**).

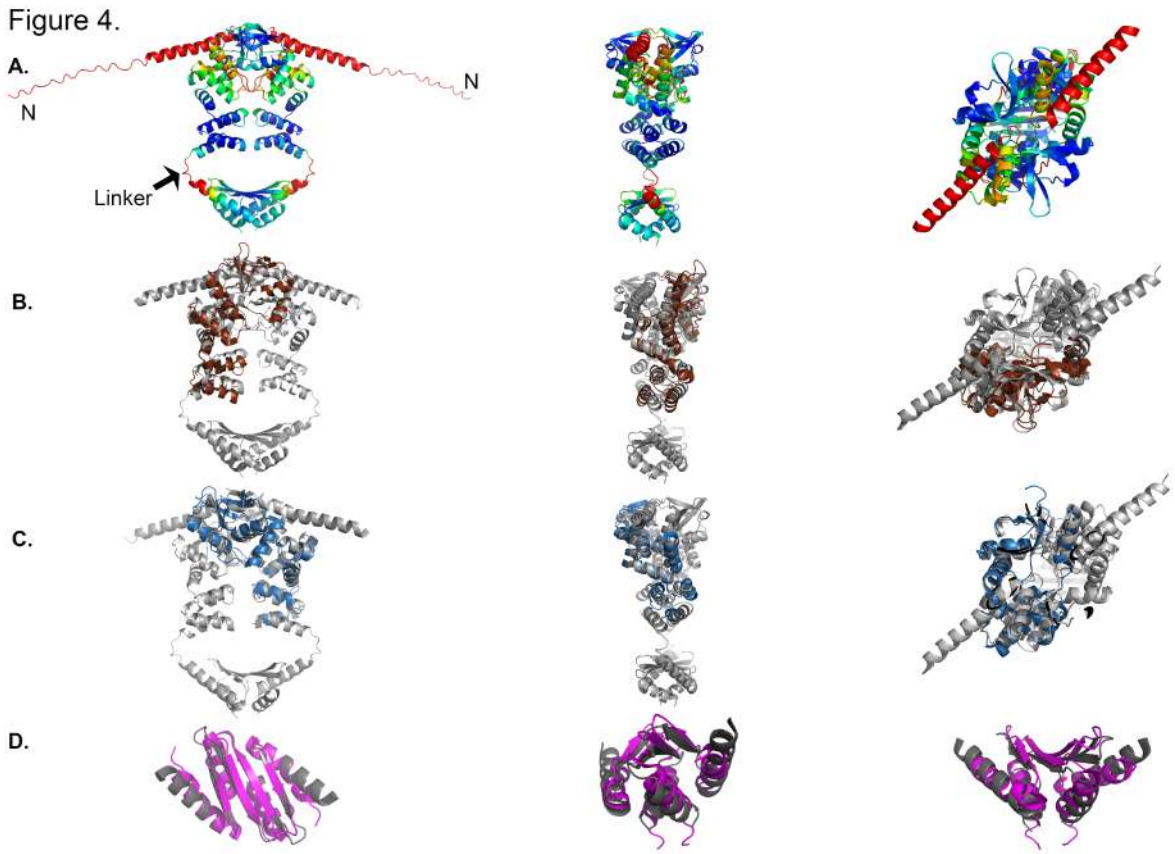

Figure 4. Alphafold multimer predicted structure of dimeric, full-length vcParB1. (A) Three views of predicted structure of vcParB1 colored according to the pLDDT score (90 to 50, blue to red) in cartoon. (B-C) Three different views of the predicted structures of vcParB1 (grey, the N-terminal disordered region is not shown) superposed with (B) *parS1*-bound cvParBtrunc (brown, pdb code: 6t1f, RMSD 3.4 Å for 182 Cα atoms aligned), (C) a nucleotide-bound form of cvParBtrunc (light blue, pdb code: 7bm8, RMSD 2.2 Å for 171 Cα atoms aligned). (D) The dimeric CTDD region of predicted vcParB1 (grey cartoon) aligned with a model of the C-terminal domain of bsParB (magenta cartoon, pdb code: 5noc, RMSD 1.5 Å for 48 Cα atoms aligned). All figures show Alphafold2 structures of vcParB1 predicted using the nucleotide-bound form of cvParBtrunc (pdb code 7bm8) as a custom template, except 4B. In 4B, the Alphafold2 structure of vcParB1 that was predicted using *parS1*-bound cvParBtrunc (pdb code 6t1f) as a custom template is shown.

3. Integrative structural modelling of full-length vcParB1-*parS1* nucleoprotein assembly

Even though crystal structures of truncated domains of ParB, ParB-nucleotide and ParB-*parS* complexes yielded valuable insights into the ParB DNA clamping mechanism (Osorio-Valeriano et al., 2019; Soh et al., 2019; Jalal et al., 2020; Jalal et al., 2021; Osorio-Valeriano et al., 2021), structural models of full-length ParB, and ParB-*parS* complex, are required to fully comprehend the mechanism of the clamping cycle. Probably due to the presence of IDRs, full-length crystal structures of ParBs are still not available. We used Alphafold multimer V3, as available in colabfold (Mirdita et al., 2022), with custom templates of truncated cvParB (Jalal et al., 2021), to obtain models of full-length predicted structures of dimeric vcParB1 (**Figure 4A**). Predicted structures of CTPBD and HTHD of vcParB1 were similar to the template structures of truncated cvParB (**Figure 4B-C;** Jalal et al., 2021). Predicted structure of C-terminal dimeric CTDD was strikingly similar to the NMR structures of the dimeric C-terminal domain of ParB (Spo0J) from *B. subtilis* (pdb code 5noc, Fisher et al., 2017), with which it bears very low sequence identity (**Figure 4D**). Poorly defined segments with low pLDDT scores in these Alphafold2 structures, one in the N-terminal region and another short linker joining CTPBD and HTHD, appear to correlate well with predicted IDR regions (**Figures 2B, 4A**). However, the AI-predicted structure of vcParB1 appear to be in an “N-gate closed” form. Calculated SAXS profile obtained from the AI-predicted model of vcParB1 as such does not match any of the experimental, averaged SEC-SAXS profiles (**Figure S5**). Docking a *parS1* DNA at the HTHD of this dimeric AI-predicted structure of vcParB1 will create steric conflict. To obtain open and DNA-bound conformations of full-length vcParB1 from the predicted structure, alterations will be required.

Figure 5.

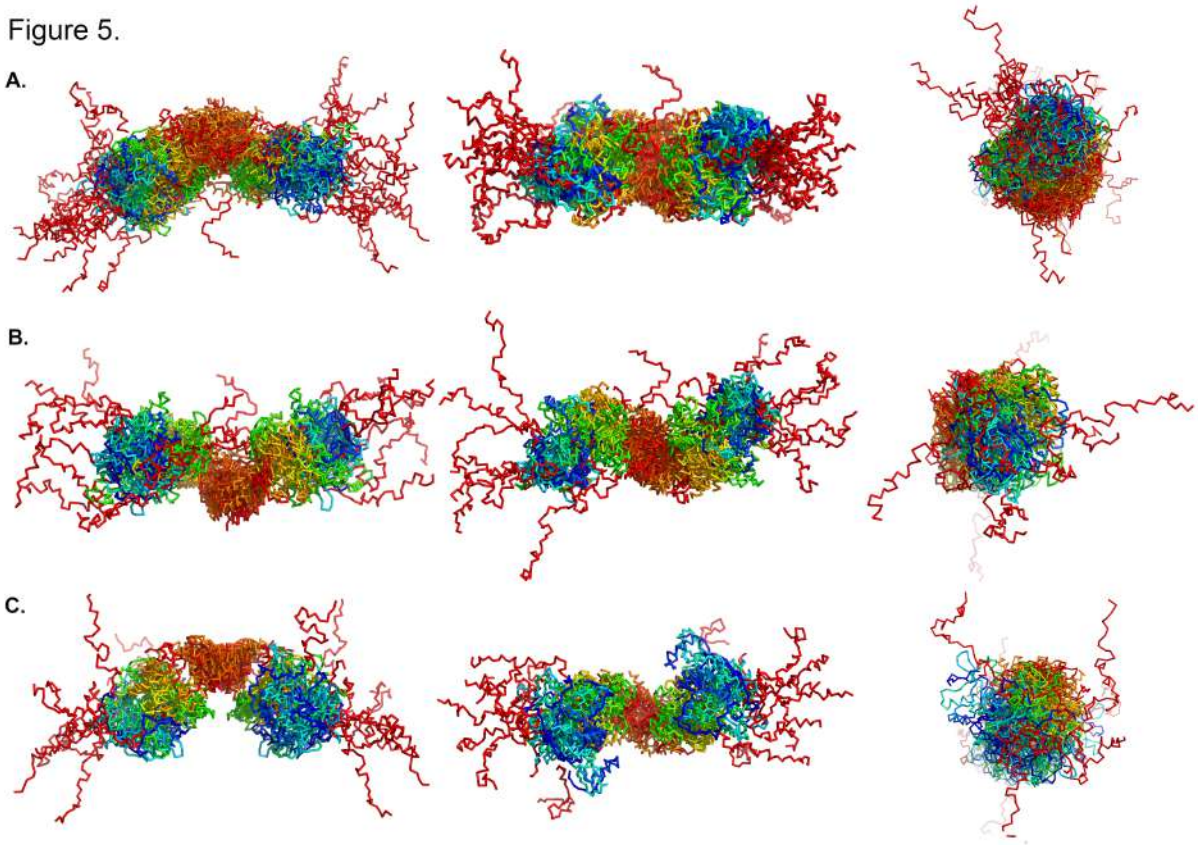

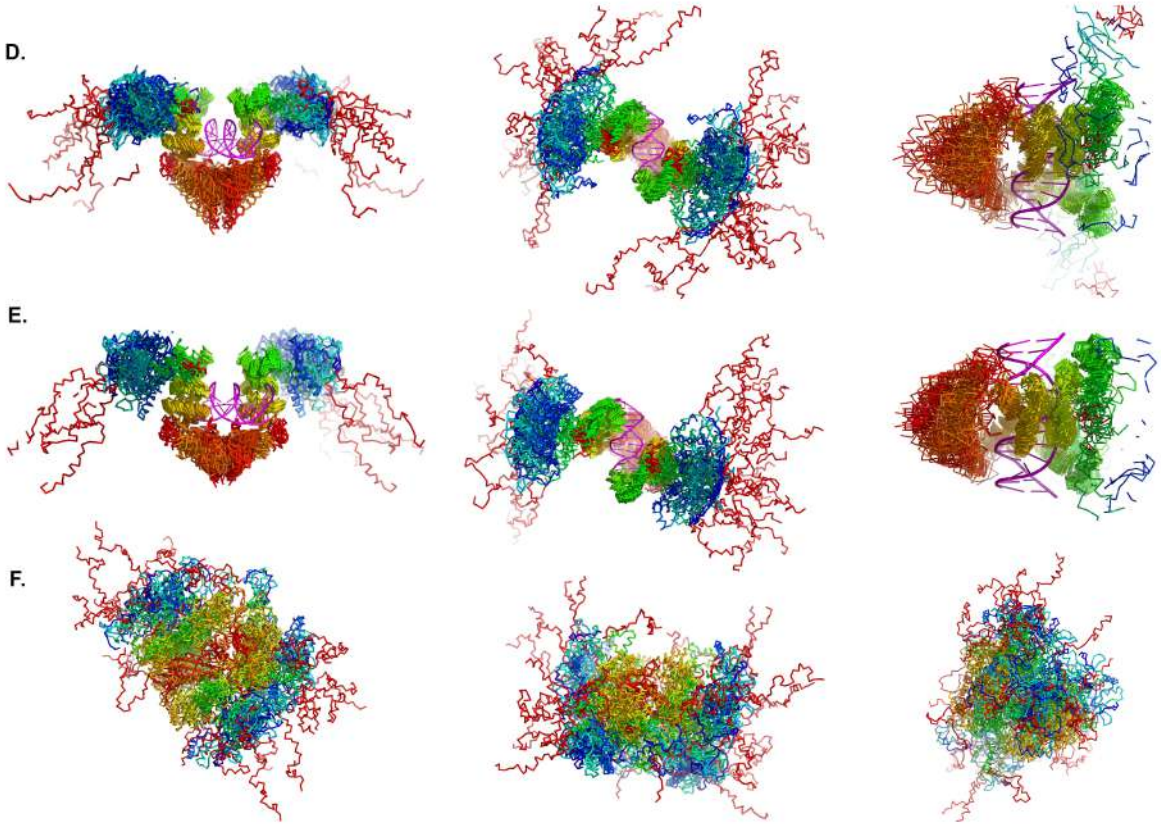

Figure 5. Integrative or hybrid structural models of vcParB1 and vcParB1-*parS1* assembly. Three different views of (A) 20 superposed hybrid structures of vcParB1 (vcParB1-peak data), (B) 10 superposed hybrid structures of vcParB1 cluster I, (C) 10 superposed hybrid structures of vcParB1 cluster II, (D) 20 superposed hybrid structures of vcParB1-*parS1* (vcParB1-*parS1*-peak data), (E) 20 superposed hybrid structures of vcParB1-*parS1* (vcParB1-*parS1*-deconv data), (F) 20 superposed hybrid structures of vcParB1 (vcParB1-CTP-peak data). All structures are shown in ribbon (in rainbow, except the N-terminal flexible region, which is shown in dark-red). The dimeric CTDD is centrally located in all the figures, and is used for alignment in figures 5A-C and F. The structure of *parS1* was kept fixed during the modelling of vcParB1-*parS1* complexes, which are shown without alignment in figure 5D-E.

To obtain the average solution structures of full-length vcParB1 and vcParB1-*parS1* assembly, we used an integrative modelling approach implemented in the CORAL program of the ATSAS suite (Petoukhov et al., 2012). The AI-predicted structures of rigid domains of vcParB1 (and *parS1* for the nucleoprotein assembly) were combined with experimental SAXS data, synthetic SAXS data based on prior knowledge of domain interfaces, 2-fold symmetry constraints, and additional distance restraints, for structural modelling (described in the methods section). Structural models corresponding to vcParB1-peak, vcParB1-*parS1*-peak and vcParb1-parS1-deconv datasets were obtained with good fit to the average SAXS profiles (**Figure 5A-F; Figure S6, S7**). 20 hybrid structures of vcParB1 were

clustered into two groups by manual inspection (cluster I and cluster II; 10 structures in each cluster; **Figure 5B-C**), that are not distinguishable by our low-resolution SAXS-based modelling scheme. On average, vcParB1 appears to be in a V-shaped conformation in solution.

Integrative modelling of vcParB1-*parS1* complex based on vcParB1-*parS1*-peak and vcParB1-*parS1*-deconv datasets provided consistent structural models (**Figure 5D-E)**. These *parS1*-bound hybrid models of vcParB1 contain a lumen region surrounded by the HTHD, linker region and CTDD. The size of the lumen varies amongst the hybrid structures from different runs. The two CTPBD are not in "N-gate closed" form or as close as they are in the crystal structure of cvParB1trunc-*parS* complex (pdb code: 6t1f). An attempt to model vcParB1-*parS1* complex with distance restraints to bring the CTPBD closer led to high χ^2 values (**Figure S6D**).

Much conformational variability was observed in the hybrid models of CTP-treated vcParB1 from different CORAL runs (**Figure 5F**, **Figure S6E**), and therefore not discussed further. CORAL runs with "N gate closed" condition imposed as additional synthetic data produced hybrid models of nucleotide-bound vcParB1 with very high χ^2 values (**Figure S6F**, see methods section). Therefore, we concluded that the CTP-treated vcParB1 is in an "N-gate" open conformation in solution.

4. A truncated form of vcParB1 devoid of the intrinsically unstructured regions is highly heterogeneous

Quite unexpectedly, the SEC-SAXS elution profile of vcParB1trunc showed noticeable heterogeneity (**Figure 6A**). Distribution of R_g around the peak regions in vcParB1trunc showed a distinct slope, indicating the presence of multiple types of scattering particles that are being separated while eluting (**Figure 6A;** Martin et al., 2021l). SVD analysis suggested presence of multiple components in the eluted peak of vcParB1trunc (**Figure 6B**). A SEC run with vcParB1trunc at ~ 375 μM concentration, which is comparable to the concentration of vcParB1trunc injected to the SEC-SAXS column (~ 386 μM), showed elution of multiple peaks that were not well-resolved (data not shown). This trimmed vcParB1trunc containing the CTPBD and the HTHD showed both CTP hydrolytic and DNA binding abilities (**Figure 2**). As it was not possible to obtain an averaged SEC-SAXS profile of vcParB1trunc due to large variation in R_g across the peak, a number of SAXS profiles averaged over a few frames from different sections of the eluted peak of vcParB1trunc were used for further analysis (**Figure S8**). These segments of the eluted peak were sequentially numbered from I to VI (from left, early eluting to right, late eluting). Kratky plots obtained from these SAXS profiles suggested presence of folded proteins (**Figure 6C**). Comparison of pair distribution functions obtained from these SAXS profiles, with a large variation in D_{max}, further supported high level of heterogeneity in vcParB1trunc (**Figure 6D**).

Figure 6.

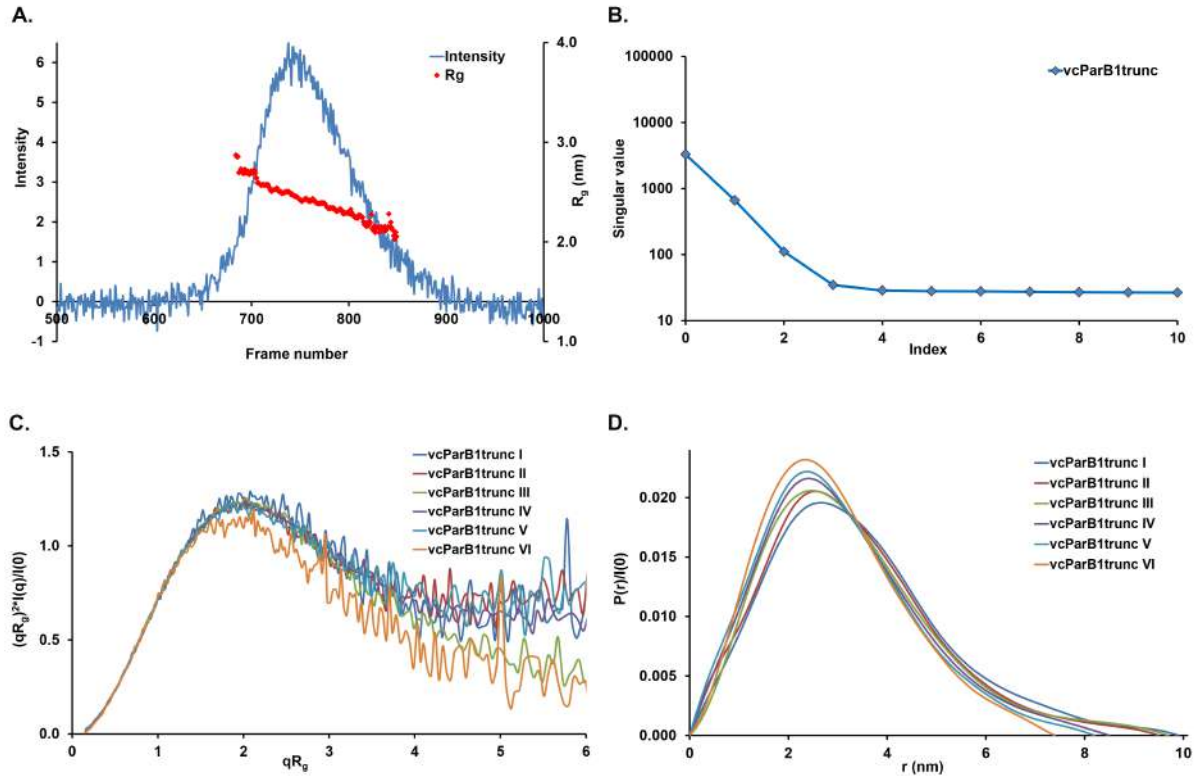

Figure 6. Structural heterogeneity in vcParB1trunc. (A) SEC-SAXS elution profile of vcParB1trunc with integrated intensity (primary vertical axis, blue line, arbitrary unit) and moving average R_g over 5 frames (secondary vertical axis, red diamond, in nm) *versus* frame numbers. (B) Result of singular value decomposition of the vcParB1trunc SEC-SAXS dataset encompassing the peak region. Semilog plot of singular value *versus* index is shown. (C) Dimensionless Kratky plots, $(qR_g)^2I(q)/I(0)$ *versus* qR_g (I(q) is intensity in arbitrary unit and q is momentum transfer), and (D) normalized pair-distribution functions (normalized by forward scattering intensity) of averaged SAXS profiles of segments obtained from the above dataset, with segment ranges I to VI (early to late eluting segments). Pair distribution functions were calculated and shown as described in figure 3B.

According to previous reports, CTPBD of ParBs can oligomerize in multiple ways (Soh et al., 2019; Chen et al., 2015). The CTPBD of ParB can dimerize with two nucleotides bound at the interface (Soh et al., 2019). In addition, a tetrameric form of CTPBD reportedly participates in DNA bridging (Chen et al., 2015). On the other hand, the HTHD of ParB can only dimerize in the presence of *parS* DNA (Jalal et al., 2020; Jalal et al., 2021). SVD analysis of the SEC-SAXS data suggests that the eluted vcParB1trunc peak contain 3 significant components (**Figure 6B**). Large variation in particle size observed for vcParB1trunc is most likely due to the presence of a mixture of oligomers in solution that are formed by intermolecular self-association.

5. Elevating flexibility in the linker region promotes self-association of vcParB1

Next, we asked, what molecular features could be responsible for balancing between the intra-molecular clamp formation within the dimeric vcParB1 and intermolecular self-association that is presumably required for higher order partition assembly formation? A short flexible linker region has been identified in many ParB homologs that join the CTDD and HTHD (**Figure 2A-B**; **Figure 7A**). A number of predicted full-length ParB structures downloaded from the Alphafold2 database (alphafold.ebi.ac.uk) showed very low pLDDT score in this linker region, further supporting predicted flexibility in this region (**Figure 7B**). We hypothesized that this linker is restricting the N-terminal region of wild-type vcParB1 dimer from self-interaction with neighbouring dimers by limiting the rotational freedom around the linker (**Figure 7C**). To test this hypothesis, we designed a triple mutant (vcParB1-linker; P235G, D237G, K239A, **Figure 7A**) to impart elevated conformational flexibility in this linker region. We expect that a highly flexible linker will allow the N-terminal segment of vcParB1 to liberally rotate about the linker to sample wider conformational space, thus enhancing chances of intermolecular interactions compared to the wild-type.

Figure 7.

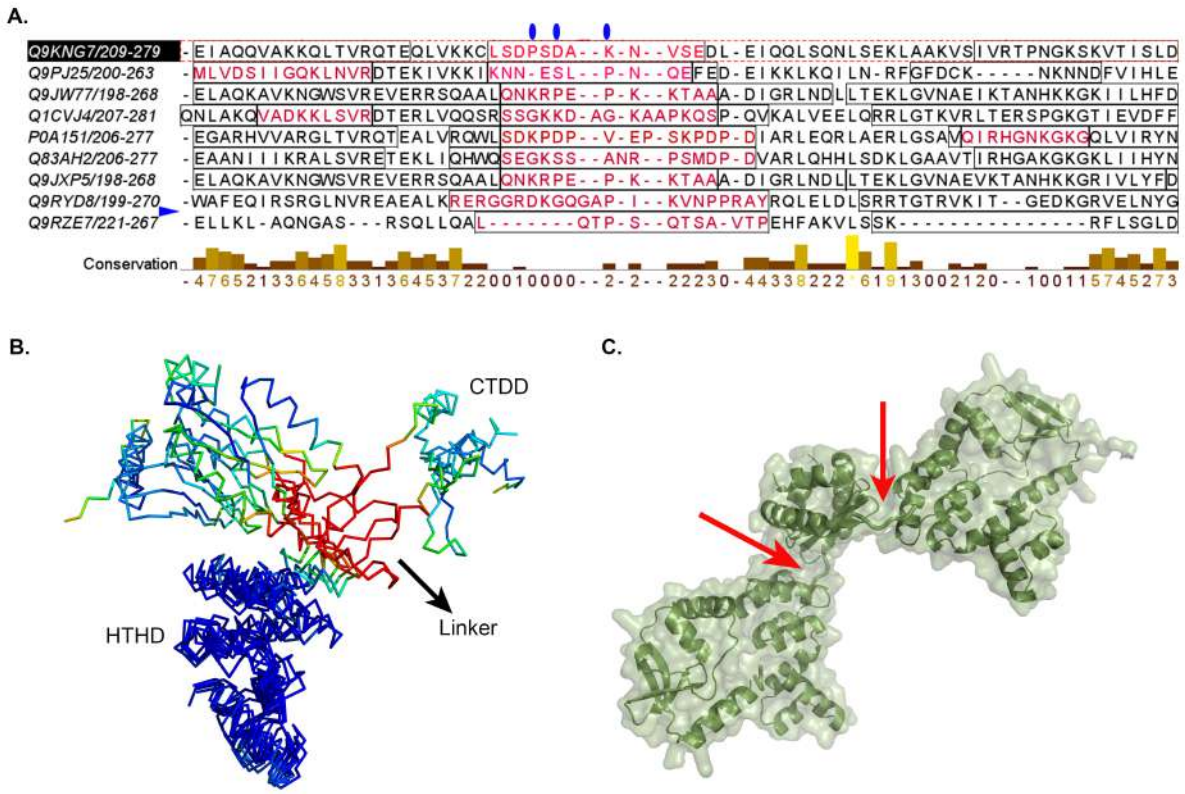

Figure 7. The linker region of vcParB1 is a putative intrinsically unstructured region. (A) Multiple sequence alignment of the linker region of vcParB1 (Uniprot accession number: Q9KNG7, residues 209-279) and other ParB homologs (Uniprot accession numbers: Q9PJ25, Q9JW77, Q1CVJ4, P0A151, Q83AH2, Q9JXP5, Q9RYD8, Q9RZE7) is shown with predicted flexibility (hot loop, coloured in red, Linding *et al*, 2003). Sequence conservation scores are shown below the sequence alignment. The positions of the three mutations in vcParB1-linker construct are marked with blue stars. (B) Superposed Alphafold2 predicted structures of vcParB1 and ParB

homologs (Uniprot accession numbers: Q9PB63, Q9RYD8, Q87BY1, Q92JI0, Q1CVJ4, Q9JW77), coloured by pLDDT score (90 in blue to 50 in red), are shown. Predicted structures were superimposed using the Cα atoms of the HTHD. The CTPBD are not shown. (C) A hybrid structural model of dimeric vcParB1 is shown as cartoon (green), with semi-transparent surface. Two linker regions are marked with red arrows.

To compare self-associating properties of wild-type vcParB1 and triple mutant vcParB1-linker, we obtained batch-mode SAXS data. Dimensionless Kratky plots obtained from these SAXS data suggested high level of self-association (as opposed to self-avoiding behaviour, Martin et al., 2021) in the vcParB1 constructs (**Figure 8A**). In addition, pair distribution function plots of these vcParB1 and vcParB1-linker SAXS profiles showed large variation in D_{max}, and notably higher D_{max} than that obtained from vcParB1-peak data, which is an indication of higher order oligomerization (**Figure 8B**). Maximum particle diameters obtained from the vcParB1-linker datasets were more-or-less consistently higher than that from the vcParB1 datasets, suggesting higher degree of self-association in the linker mutant (**Figure 8B**). To quantitate self-interaction in wild-type vcParB1 and mutant vcParB1-linker, we calculated second virial coefficient (B22) from batch-mode SAXS data (Pabit et al., 2009). B22 for vcParB1 and vcParB1-linker were estimated to be - 3.99 X 10^{-4} mol.mL.g^{-2} and - 4.66 X 10^{-4} mol.mL.g^{-2}, respectively. Negative B22 values imply attractive interaction, and it appears from the B22 values that the vcParB1-linker is somewhat more association-prone than vcParB1 within our experimental concentration regime. Thus, imparting more flexibility in the short intrinsically unstructured linker region joining the CTDD and HTHD made full-length vcParB1 highly association-prone.

Figure 8.

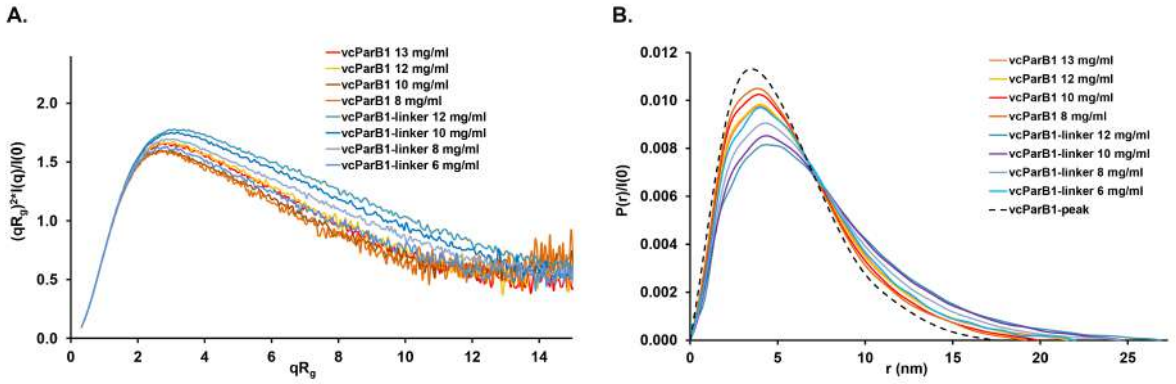

Figure 8. SAXS data suggests that vcParB1-linker triple mutant is more association-prone than the wild-type vcParB1. (A) Dimensionless Kratky plots (as described in figure 6C) and (B) pair-distribution function plots (as described in figure 3B) of SAXS concentration series obtained from vcParB1 and vcParB1-linker. Real space R_g and forward scattering intensity values obtained from the pair-distribution function were used for calculating the Kratky plots. Pair distribution function obtained from the vcParB1-peak SEC-SAXS data is shown as dashed black line for comparison in figure 8B.

6. Conformational states of vcParB1

The AI-predicted structure of vcParB1, which is in “N-gate” closed form, was compared with the hybrid structures of vcParB1 and vcParB1-*parS1* assembly that were built based on experimental and synthetic data (**Figure 9A-B**). Unbound vcParB1 adopted open V-shaped forms in solution (**Figure 5A-C**). It was not possible to obtain consistent structural models of the CTP-treated vcParB1. However, high χ^2 values associated with the structural models of vcParB1-CTP that were obtained when “N-gate” closure conditions were imposed clearly suggested that it was not in an “N-gate closed” form in solution (**Figure 5F**, **Figure S6F**). This result agrees with the expectation that considering the cytosolic concentration of CTP in bacteria (~ 0.3 mM, Buckstein et al., 2008), majority of intracellular ParB will be likely in CTP-bound, “N-gate” open form (Osorio-Valeriano et al., 2019).

Figure 9.

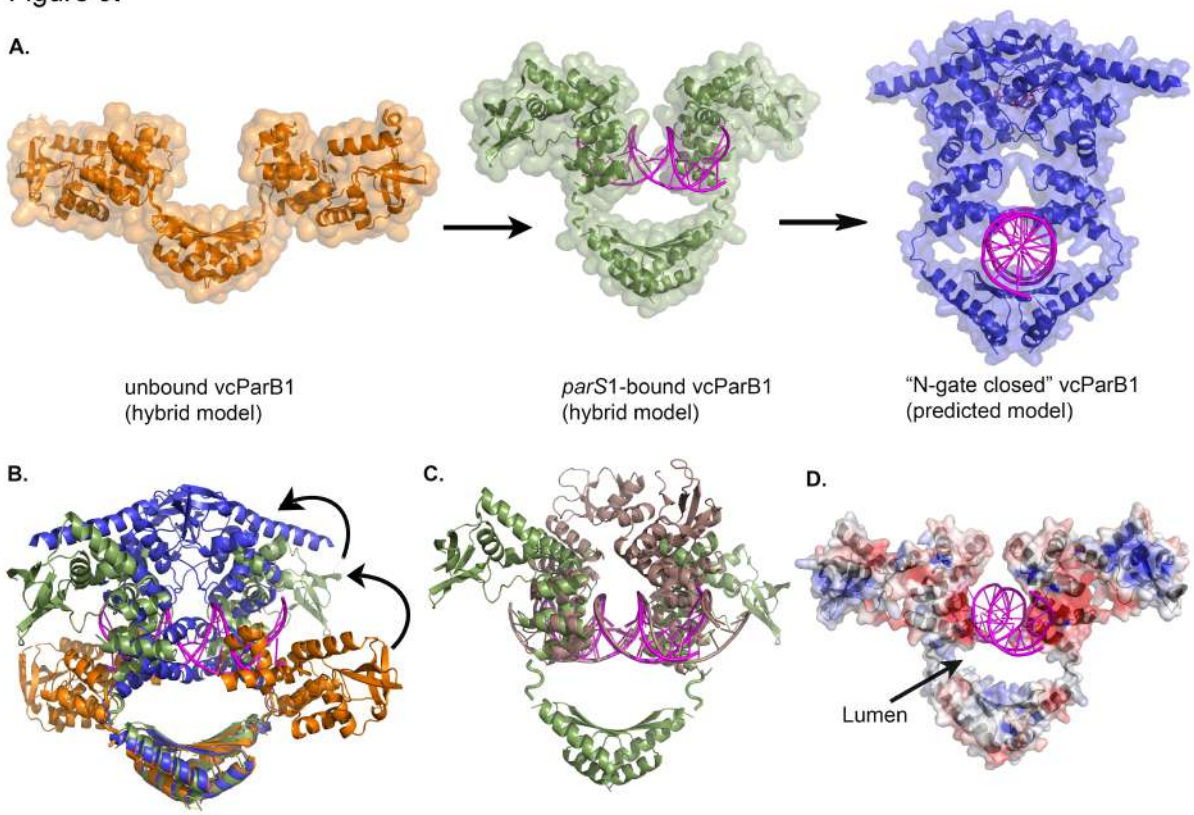

Figure 9. Conformational states of vcParB1. (A) Representative hybrid models of a vcParB1 dimer in orange and a vcParB1-*parS1* complex in green, with *parS1* in magenta, are shown as cartoons. AI-predicted structure of vcParB1 in “N-gate closed” form (blue) is shown as a cartoon. Two docked nucleotides in the CTPBD (red sticks), and a *parS1* DNA docked in the lumen region (magenta) are shown with the predicted structure of vcParB1. The *parS1* DNA is tightly fitted in the lumen, with steric conflicts. Further conformational changes in the lumen will be required to accommodate the sliding DNA. Semi-transparent surfaces are shown along with the cartoons. (B) Superposed representative structures of integrative models of vcParB1

(orange), vcParB1-*parS1* (green, *parS1* in magenta) and AI-predicted vcParB1 (blue) are shown. The CTDD (residues 239-293) was used for structural alignment in Coot (Emsley and Cowtan, 2004). Black curly arrows show the movement of CTPBD between different conformational states of vcParB1. (C) Cartoons of a hybrid structure of full-length vcParB1-*parS1* (green, *parS1* in magenta,) superposed on the truncated crystal structure of cvParBtrunc-*parS* complex (pink, superposed using the HTHD, Jalal et al., 2021). (D) Electrostatic potential (calculated using APBS, Baker et al., 2001) mapped on the surface of vcParB1-*parS1* (shown as a semi-transparent surface, along with the cartoon of the structure in grey). The secondary DNA-binding site of CTDD is positioned exactly below *parS1*, which is lining the lumen. The flexible N-terminal region is not included in the cartoons for clarity.

Hybrid models of vcParB1-*parS1* complex showed large *parS1*-induced movement of the CTPBD, which brings them closer in space in comparison to the open forms of vcParB1 (**Figure 5D-E**; **Figure 9A-B**). The *parS1*-induced repositioning of the CTPBD probably facilitates subsequent "N-gate" closure, and dislodging of *parS1* to the lumen upon nucleotide binding (**Figure 9A-B**). Unlike in our hybrid models, the CTPBD domains in the crystal structure of *parS*-bound truncated cvParB are in physical proximity (**Figure 9C**). Crystallization probably favoured compact form of ParB-*parS*. Such compact forms could be lowly populated, or transiently formed in solution, and therefore not captured by our average solution structure modelling approach. The CTPBD in our hybrid models of vcParB1-*parS1* dimer will be available for either intramolecular (clamping) or intermolecular (condensing) interactions.

Binding of DNA induced formation of a lumen region in vcParB1 (**Figure 9D**). The secondary DNA binding site of the vcParB1, which is in the CTDD, is suitably positioned below the lumen for capturing the displaced *parS1* upon "N-gate" closure (**Figure 9D**). Together, these conformational states delineated a probable pathway for *parS1*-induced changes in vcParB1 that can lead to subsequent "N-gate" closure and sliding of the clamp.

Discussion

Since the recent serendipitous discovery that ParB is a CTP switch and a DNA clamp, number of CTP switches reported in the literature is steadily growing (McLean. and Le, 2023). However, domain rearrangements involving formation and breakdown of inter-domain interfaces that describe CTP switching and DNA clamping actions of ParB are not fully understood, and necessitates characterization of the key conformations of full-length ParB in various states.

We combined domains obtained from AI-predicted structures of multi-domain and multimeric vcParB1 with experimental SEC-SAXS data to model conformational states of full-length vcParB1 and vcParB1-*parS1* (**Figure 5**). Calculated SAXS profiles of individual domain dimers of CTDD, HTHD and CTPBD were used as additional synthetic data for modelling different conformational states. In addition, distance restraints were used to maintain known protein-protein, and DNA-protein, interaction interfaces during structural modelling. Even though such structural models built using sparse data are not suitable for fine structural analysis, they can

be powerful reporters of domain movements and domain interface formation. Resultant average solution structures of vcParB1 in DNA-bound and DNA-free forms suggested DNA-induced conformational change in vcParB1 that aided in mechanistic understanding of vcParB1-DNA clamping process (**Figure 9**). In our structural models, the two CTPBD domains where moved nearer upon ParB1-*parS1* assembling, and a lumen poised for capturing the dislodged *parS1* was formed in ParB1 beneath the bound DNA, thus priming the ParB1 clamp for sliding.

Quite unexpectedly, the removal of intrinsically unstructured components, and CTDD, made a truncated construct of vcParB1 association-prone (**Figure 6A-D**). We note that SAXS is a weight-average method and presence of a small amount of higher order oligomer can change the SAXS profile significantly. The observed oligomer-forming propensity of vcParB1trunc, which is folded and functional (**Figure 2 and Figure 6**), could be intrinsic in nature. Or, it could be due to the presence of small amount of co-purified CTP co-factor. However, vcParB1trunc is an active CTP hydrolyzing enzyme (**Figure 2**), which is purified using three columns before being concentrated for the SEC-SAXS experiment. Therefore, it is quite likely that vcParB1trunc is intrinsically oligomerization-prone, which is probably boosted in the presence of CTP. Since local concentration of ParBs can be as high as 500 μM within the partition assembly (Lim et al., 2014), observed protein-protein self-associating property of vcParB1trunc in the SEC-SAXS run at high concentration might be relevant for partition assembly condensate formation.

Mutational analysis suggests that the linker region joining the HTHD and CTDD is curbing the higher order self-assembling of vcParB1 dimer, probably by making the interaction interfaces of the N-terminal segments less accessible for intermolecular interactions (**Figure 7, 8**). Like other ParBs (Guilhas et al., 2020; Babl et al., 2022), vcParB1 form condensates (unpublished results). Therefore, self-associating propensity of vcParB1 is hardly surprising. Observed self-association of vcParB1 constructs is likely linked to its ability to form higher order partition assembly condensate under favourable cellular conditions. The linker region probably helps to keep vcParB1 in clamping-ready dimeric state. On the other hand, within the highly crowded partition assembly, higher order self-association of vcParB1 might prevail to aid in the formation and maintenance of the partition assembly. It appears that CTP is a driver of ParB LLPS formation (Babl et al., 2022). How the clamping-sliding functions and DNA-bridging functions of ParBs are combined for partition assembly formation, and how CTP supports these processes, are key questions remains to be answered.

Acknowledgements

BC wishes to thank the Department of Biotechnology (DBT), Govt. of India, for an extramural grant (BT/PR8804/BRB/10/1252/2013) and Council of Scientific and Industrial Research (CSIR), Govt. of India, for intramural funding to support this project. BC thanks CSIR support and institutional facility. All SAXS data were collected at beamline BM29 at ESRF, France, which was supported by DBT and administered by Regional Centre of Biotechnology, Faridabad. We thank BM29 staff members for help during SAXS and SEC-SAXS data collection. Anu thanks CSIR for her fellowship. Sneh Lata thanks Indian Council of Medical Research for her fellowship.

Tables

Table 1. Data collection parameters for SAXS and SEC-SAXS experiments.

Parameters	**SAXS**
Experimental station	BM29, ESRF
Wavelength (Å)	0.999
Detector distance (m)	2.81
Exposure time (sec)	1 *per* frame (10 frames)
Protein buffer	20 mM Tris pH 7.5,100 mM NaCl, 5% glycerol, 1 mM EDTA, 5mM BME, 5mM $MgCl_2$
	SEC-SAXS
Experimental station	BM29, ESRF
Wavelength (Å)	0.999
Detector distance (m)	2.81
Exposure time (sec)	2 *per* frame, ~1000 frames
SEC SAXS setup	AKTA Ettan system (GE healthcare)
SEC column	Superdex200 increase 3.2/300
Running buffer	20 mM Tris pH 7.5, 100 mM NaCl, 5% glycerol, 1 mM EDTA, 5 mM BME, 5 mM $MgCl_2$ (1.2 mM CTP added in buffer for the experiments with CTP-treated protein)

Table 2. SEC-SAXS data analysis (analysed in BioXTAS RAW, Hopkins, 2024).

Dataset	**Guinier R_g (nm)**	**q.R_g range[a]**	**Real space R_g (nm)**	**D_{max} (nm)**
vcParB1-peak	4.05 (± 0.03)	0.5 - 1.27	4.34 (±0.03)	17.0
vcParb1-*parS1*-peak	3.89 (±0.05)	0.56 - 1.3	4.16 (±0.04)	15.0
vcParB1-*parS1*-deconv	3.83 (±0.04)	0.47 -1.28	4.05 (±0.04)	15.0
vcParB1-CTP-peak	3.93 (±0.04)	0.525 - 1.29	4.24 (±0.05)	16.0

a – qR_g range for Guinier R_g calculations. D_{max} values are rounded off.

References

Alberstein, R.G., Guo, A.B. and Kortemme, T. (2022) Design principles of protein switches. *Curr Opin Struct Biol*, **72**, 71-78.

Antar, H., Soh, Y.M., Zamuner, S., Bock, F.P., Anchimiuk, A., De los Rios, P. and Gruber, S. (2021) Relief of ParB autoinhibition by DNA catalysis and recycling of ParB by CTP hydrolysis promote bacterial centromere assembly. *Sci Adv*, **7**.

Azaldegui, C.A., Vecchiarelli, A.G. and Biteen, J.S. (2021) The emergence of phase separation as an organizing principle in bacteria. *Biophys J*, **120**, 1123-1138.

Babl, L., Giacomelli, G., Ramm, B., Gelmroth, A.K., Bramkamp, M. and Schwille, P. (2022) CTP-controlled liquid-liquid phase separation of ParB. *J Mol Biol*, **434**, 167401.

Balaguer, F.A., Aicart-Ramos, C., Fisher, G.L., de Braganca, S., Martin-Cuevas, E.M., Pastrana, C.L., Dillingham, M.S. and Moreno-Herrero, F. (2021) CTP promotes efficient ParB-dependent DNA condensation by facilitating one-dimensional diffusion from parS. *Elife*, **10**.

Baker, N.A., Sept, D., Joseph, S., Holst, M.J. and McCammon, J.A. (2001) Electrostatics of nanosystems: Application to microtubules and the ribosome. *P Natl Acad Sci USA*, **98**, 10037-10041.

Bock, F.P., Liu, H.W., Anchimiuk, A., Diebold-Durand, M.L. and Gruber, S. (2022) A joint-ParB interface promotes Smc DNA recruitment. *Cell Rep*, **40**, 111273.

Brookes, E., Rocco, M., Vachette, P. and Trewhella, J. (2023) AlphaFold-predicted protein structures and small-angle X-ray scattering: insights from an extended examination of selected data in the Small-Angle Scattering Biological Data Bank. *J Appl Crystallogr*, **56**, 910-926.

Buckstein, M.H., He, J. and Rubin, H. (2008) Characterization of nucleotide pools as a function of physiological state in Escherichia coli. *J Bacteriol*, **190**, 718-726.

Chen, B.W., Lin, M.H., Chu, C.H., Hsu, C.E. and Sun, Y.J. (2015) Insights into ParB spreading from the complex structure of Spo0J and parS. *Proc Natl Acad Sci U S A*, **112**, 6613-6618.

Emsley, P. and Cowtan, K. (2004) Coot: model-building tools for molecular graphics. *Acta Crystallogr D Biol Crystallogr*, **60**, 2126-2132.

Fisher, G.L., Pastrana, C.L., Higman, V.A., Koh, A., Taylor, J.A., Butterer, A., Craggs, T., Sobott, F., Murray, H., Crump, M.P. *et al.* (2017) The structural basis for dynamic DNA binding and bridging interactions which condense the bacterial centromere. *Elife*, **6**.

Fogel, M.A. and Waldor, M.K. (2005) Distinct segregation dynamics of the two Vibrio cholerae chromosomes. *Mol Microbiol*, **55**, 125-136.

Funnell, B.E. (2016) ParB Partition Proteins: Complex Formation and Spreading at Bacterial and Plasmid Centromeres. *Front Mol Biosci*, **3**, 44.

Guilhas, B., Walter, J.C., Rech, J., David, G., Walliser, N.O., Palmeri, J., Mathieu-Demaziere, C., Parmeggiani, A., Bouet, J.Y., Le Gall, A. *et al.* (2020) ATP-Driven Separation of Liquid Phase Condensates in Bacteria. *Mol Cell*, **79**, 293-303 e294.

Guo, L., Zhao, Y., Zhang, Q., Feng, Y., Bi, L., Zhang, X., Wang, T., Liu, C., Ma, H. and Sun, B. (2022) Stochastically multimerized ParB orchestrates DNA assembly as unveiled by single-molecule analysis. *Nucleic Acids Res*, **50**, 9294-9305.

Hopkins, J.B. (2024) BioXTAS RAW 2: new developments for a free open-source program for small-angle scattering data reduction and analysis. *J Appl Crystallogr*, **57**, 194-208.

Jalal, A.S., Tran, N.T. and Le, T.B. (2020) ParB spreading on DNA requires cytidine triphosphate in vitro. *Elife*, **9**.

Jalal, A.S., Tran, N.T., Stevenson, C.E., Chimthanawala, A., Badrinarayanan, A., Lawson, D.M. and Le, T.B. (2021) A CTP-dependent gating mechanism enables ParB spreading on DNA. *Elife*, **10**.

Jalal, A.S.B. and Le, T.B.K. (2020) Bacterial chromosome segregation by the ParABS system. *Open Biol*, **10**, 200097.

Jalal, A.S.B., Tran, N.T., Stevenson, C.E., Chan, E.W., Lo, R., Tan, X., Noy, A., Lawson, D.M. and Le, T.B.K. (2020) Diversification of DNA-Binding Specificity by Permissive and Specificity-Switching Mutations in the ParB/Noc Protein Family. *Cell Rep*, **32**, 107928.

Jumper, J., Evans, R., Pritzel, A., Green, T., Figurnov, M., Ronneberger, O., Tunyasuvunakool, K., Bates, R., Zidek, A., Potapenko, A. *et al.* (2021) Highly accurate protein structure prediction with AlphaFold. *Nature*, **596**, 583-589.

Liebschner, D., Afonine, P.V., Baker, M.L., Bunkóczi, G., Chen, V.B., Croll, T.I., Hintze, B., Hung, L.W., Jain, S., McCoy, A.J. *et al.* (2019) Macromolecular structure determination using X-rays, neutrons and electrons: recent developments in Phenix. *Acta Crystallogr D Struct Biol*, **75**, 861-877.

Lim, H.C., Surovtsev, I.V., Beltran, B.G., Huang, F., Bewersdorf, J. and Jacobs-Wagner, C. (2014) Evidence for a DNA-relay mechanism in ParABS-mediated chromosome segregation. *Elife*, **3**, e02758.

Linding, R., Jensen, L.J., Diella, F., Bork, P., Gibson, T.J. and Russell, R.B. (2003) Protein disorder prediction: implications for structural proteomics. *Structure*, **11**, 1453-1459.

Livny, J., Yamaichi, Y. and Waldor, M.K. (2007) Distribution of centromere-like parS sites in bacteria: insights from comparative genomics. *J Bacteriol*, **189**, 8693-8703.

Manalastas-Cantos, K., Konarev, P.V., Hajizadeh, N.R., Kikhney, A.G., Petoukhov, M.V., Molodenskiy, D.S., Panjkovich, A., Mertens, H.D.T., Gruzinov, A., Borges, C. *et al.* (2021) ATSAS 3.0: expanded functionality and new tools for small-angle scattering data analysis. *J Appl Crystallogr*, **54**, 343-355.

Martin, E.W., Hopkins, J.B. and Mittag, T. (2021) Small-angle X-ray scattering experiments of monodisperse intrinsically disordered protein samples close to the solubility limit. *Methods Enzymol*, **646**, 185-222.

Mathew, E., Mirza, A. and Menhart, N. (2004) Liquid-chromatography-coupled SAXS for accurate sizing of aggregating proteins. *J Synchrotron Radiat*, **11**, 314-318.

McLean, T.C. and Le, T.B. (2023) CTP switches in ParABS-mediated bacterial chromosome segregation and beyond. *Curr Opin Microbiol*, **73**, 102289.

Meisburger, S.P., Taylor, A.B., Khan, C.A., Zhang, S., Fitzpatrick, P.F. and Ando, N. (2016) Domain Movements upon Activation of Phenylalanine Hydroxylase Characterized by Crystallography and Chromatography-Coupled Small-Angle X-ray Scattering. *J Am Chem Soc*, **138**, 6506-6516.

Meisburger, S.P., Xu, D. and Ando, N. (2021) REGALS: a general method to deconvolve X-ray scattering data from evolving mixtures. *IUCrJ*, **8**, 225-237.

Mirdita, M., Schutze, K., Moriwaki, Y., Heo, L., Ovchinnikov, S. and Steinegger, M. (2022) ColabFold: making protein folding accessible to all. *Nat Methods*, **19**, 679-682.

Osorio-Valeriano, M., Altegoer, F., Steinchen, W., Urban, S., Liu, Y., Bange, G. and Thanbichler, M. (2019) ParB-type DNA Segregation Proteins Are CTP-Dependent Molecular Switches. *Cell*, **179**, 1512-1524 e1515.

Osorio-Valeriano, M., Altegoer, F., Das, C.K., Steinchen, W., Panis, G., Connolley, L., Giacomelli, G., Feddersen, H., Corrales-Guerrero, L., Giammarinaro, P.I. *et al.* (2021) The CTPase activity of ParB determines the size and dynamics of prokaryotic DNA partition complexes. *Mol Cell*, **81**, 3992-4007.e3910.

Pabit, S.A., Qiu, X., Lamb, J.S., Li, L., Meisburger, S.P. and Pollack, L. (2009) Both helix topology and counterion distribution contribute to the more effective charge screening in dsRNA compared with dsDNA. *Nucleic Acids Res*, **37**, 3887-3896.

Perkins, D.N., Pappin, D.J., Creasy, D.M. and Cottrell, J.S. (1999) Probability-based protein identification by searching sequence databases using mass spectrometry data. *Electrophoresis*, **20**, 3551-3567.

Petoukhov, M.V., Franke, D., Shkumatov, A.V., Tria, G., Kikhney, A.G., Gajda, M., Gorba, C., Mertens, H.D., Konarev, P.V. and Svergun, D.I. (2012) New developments in the ATSAS program package for small-angle scattering data analysis. *J Appl Crystallogr*, **45**, 342-350.

Ptacin, J.L., Lee, S.F., Garner, E.C., Toro, E., Eckart, M., Comolli, L.R., Moerner, W.E. and Shapiro, L. (2010) A spindle-like apparatus guides bacterial chromosome segregation. *Nat Cell Biol*, **12**, 791-798.

Ramachandran, R., Jha, J. and Chattoraj, D.K. (2014) Chromosome segregation in Vibrio cholerae. *J Mol Microbiol Biotechnol*, **24**, 360-370.

Sanchez, A., Cattoni, D.I., Walter, J.C., Rech, J., Parmeggiani, A., Nollmann, M. and Bouet, J.Y. (2015) Stochastic Self-Assembly of ParB Proteins Builds the Bacterial DNA Segregation Apparatus. *Cell Syst*, **1**, 163-173.

Soh, Y.M., Davidson, I.F., Zamuner, S., Basquin, J., Bock, F.P., Taschner, M., Veening, J.W., De Los Rios, P., Peters, J.M. and Gruber, S. (2019) Self-organization of parS centromeres by the ParB CTP hydrolase. *Science*, **366**, 1129-1133.

Sullivan, N.L., Marquis, K.A. and Rudner, D.Z. (2009) Recruitment of SMC by ParB-parS organizes the origin region and promotes efficient chromosome segregation. *Cell*, **137**, 697-707.

Ishida, T. and Kinoshita, K. (2007) PrDOS: prediction of disordered protein regions from amino acid sequence. *Nucleic Acids Res*, **35**, W460-464.

Tisma, M., Panoukidou, M., Antar, H., Soh, Y.M., Barth, R., Pradhan, B., Barth, A., van der Torre, J., Michieletto, D., Gruber, S. *et al.* (2022) ParB proteins can bypass DNA-bound roadblocks via dimer-dimer recruitment. *Sci Adv*, **8**.

Tisma, M., Janissen, R., Antar, H., Martin-Gonzalez, A., Barth, R., Beekman, T., van der Torre, J., Michieletto, D., Gruber, S. and Dekker, C. (2023) Dynamic ParB-DNA interactions initiate and maintain a partition condensate for bacterial chromosome segregation. *Nucleic Acids Res*, **51**, 11856-11875.

Tisma, M., Kaljevic, J., Gruber, S., Le, T.B.K. and Dekker, C. (2024) Connecting the dots: key insights on ParB for chromosome segregation from single-molecule studies. *FEMS Microbiol Rev*, **48**.

Tully, M.D., Kieffer, J., Brennich, M.E., Cohen Aberdam, R., Florial, J.B., Hutin, S., Oscarsson, M., Beteva, A., Popov, A., Moussaoui, D. *et al.* (2023) BioSAXS at European Synchrotron Radiation Facility - Extremely Brilliant Source: BM29 with an upgraded source, detector, robot, sample environment, data collection and analysis software. *J Synchrotron Radiat*, **30**, 258-266.

Vecchiarelli, A.G., Neuman, K.C. and Mizuuchi, K. (2014) A propagating ATPase gradient drives transport of surface-confined cellular cargo. *Proc Natl Acad Sci U S A*, **111**, 4880-4885.

Walter, J.C., Rech, J., Walliser, N.O., Dorignac, J., Geniet, F., Palmeri, J., Parmeggiani, A. and Bouet, J.Y. (2020) Physical Modeling of a Sliding Clamp Mechanism for the Spreading of ParB at Short Genomic Distance from Bacterial Centromere Sites. *iScience*, **23**, 101861.

Waterhouse, A.M., Procter, J.B., Martin, D.M., Clamp, M. and Barton, G.J. (2009) Jalview Version 2--a multiple sequence alignment editor and analysis workbench. *Bioinformatics*, **25**, 1189-1191.

Yamaichi, Y., Fogel, M.A., McLeod, S.M., Hui, M.P. and Waldor, M.K. (2007) Distinct centromere-like parS sites on the two chromosomes of Vibrio spp. *J Bacteriol*, **189**, 5314-5324.